Automatic quantification of matrix cracking and fiber rotation by X-ray computed tomography in shear-deformed carbon fiber-reinforced laminates

F. Sket , A. Enfedaque , C. Alton , C. González , J.M. Molina-Aldareguia , J. Llorca

A B S T R A C T

The deformation and damage mechanisms of carbon fiber-reinforced epoxy laminates deformed in shear were studied by means of X-ray computed tomography. In particular, the evolution of matrix cracking, interply delamination and fiber rotation was ascertained as a function of the applied strain. In order to provide quantitative information, an algorithm was developed to automatically determine the crack density and the fiber orientation from the tomograms. The investigation provided new insights about the complex interaction between the different damage mechanisms (i.e. matrix cracking and interply delamination) as a function of the applied strain, ply thickness and ply location within the laminate as well as quantitative data about the evolution of matrix cracking and fiber rotation during deformation.

1. Introduction

The maximum load carrying capacity of multiaxial fiber-reinforced laminates (either in tension or in compression) is normally attained at low strains and is dictated by the fracture of the plies with the fibers oriented along the loading axis. This behavior often masks that off-axis plies within the laminate (deformed in shear) show a strong non-linear behavior and can withstand very large strains before fracture [1–3]. This shear nonlinearity influences the mechanical behavior of laminates [4,5] and the mechanisms of shear deformation in composites have been studied in the past.

Matrix cracking in the fiber direction is the first failure mechanism during tensile or compressive deformation of off-axis plies in a laminate, as it was documented in $[0/45/-45/90]_s$ $[0/90/-45/45]_s$ $[\pm45/90]_s$ $[90/\pm45]_s$ and $[0/\theta/0]$s carbon and glass/epoxy laminates [6–11]. Matrix cracking leads to a reduction in stiffness and the relation between both was modeled by Kashtalyan and Soutis [12] in $[0/\theta]_s$ laminates. In addition, fiber rotation also plays an important role in the non-linear behavior of $[\pm45]_s$ laminates [13] together with interply delamination, which results from extensive cracking of adjacent plies with different fiber orientation.

While these mechanisms are well documented from the qualitative viewpoint, quantitative data on the density of matrix cracks, the extent of interply delamination and the changes in fiber orientation with strain are very limited. Optical or electron microscopy of cross-sections is very time consuming while X-ray radiography only provides 2D information and it is not possible to separate the contributions from each ply [14,15]. These limitations can be overcome with the use of X-ray computed tomography (XCT), which provides actual 3D information of the damage and microstructure in every ply from a number of X-ray radiographies obtained at different angles. In addition, it is a non-destructive technique that can be used for tracking the damage evolution in different scenarios. For instance, Wright et al. [16] studied with synchrotron tomography the interaction of damage mechanisms in a centrally notched specimen made from a carbon/epoxy laminate $[90/0]_s$ and showed through-thickness fiber breakage and intralaminar cracking in close detail. In another study, the crack evolution in a double edge notched carbon/epoxy laminate $[90/0]_s$ was determined [17] and the observations were used to set the ground for enhancing the damage prediction of a three-dimensional finite element model. Sket et al. [18] has investigated the onset and evolution of the damage in three dimensions by XCT in a notched glass fiber/epoxy cross-ply laminate subjected to

three-point bending and this information was used to determine the effective fracture resistance curve of the cross-ply laminate. Finally, Hernández et al. [19,20] have used XCT to study the effect of curing parameters on the void volume fraction, shape and spatial distribution in C/epoxy laminates manufactured by compression molding.

Within this framework, this investigation was aimed at developing automatic analysis methods capable of tracking matrix cracking and fiber rotation from tomographic data. This methodology was used to quantify the development of damage during shear deformation in each individual ply of $[\pm 45]_{2s}$ carbon fiber laminates. The evaluation is focused on the stresses necessary to nucleate cracks, the evolution of crack density and rotation of the fibers as a function of the strain.

2. Materials and mechanical characterization

The samples for the mechanical tests were obtained from panels of $300 \times 300\ mm^2$ and 1 mm in thickness. Unidirectional carbon fibers/epoxy resin T800S/M21 prepreg sheets were supplied by Hexcel®. The T800S carbon fiber (produced by Torayca®) have a nominal diameter of 5 μm and 24 K fibers per bundle. The panels were manufactured in autoclave from T800S/M21 (carbon fibers/epoxy resin) prepreg sheets with a stacking sequence $[\pm 45]_{2s}$. A standard autoclave cure cycle was applied with a maximum cure temperature of 180 °C for 120 min and a pressure of 7 bar [21]. The heating and cooling rates were set to 2 °C/min. The ply thickness was approximately 125 μm. In this paper, the different plies will be named ply 1 to ply 7, being ply 1 and 7 the outermost plies and ply 4 the central one with twice the thickness. The nominal fiber volume fraction after consolidation was 57% and the resulting thickness was 1.0 mm.

Five specimens of $200 \times 20 \times 1.0\ mm^3$ (length × depth × thickness) were machined from the laminates with the external plies at +45°. The specimens were very carefully cut by milling using a hard metal tool with drill end and cooling liquid. Very little damage was introduced during machining. Fiber glass composite tabs were fixed to the specimens borders to avoid damaging the samples with the jaws. The distance between tabs was 100 mm. Tensile tests to determine the shear response were carried out in an electromechanical universal testing machine (Instron 3384) at constant cross-head speed of 0.6 mm/min. Load was monitored with a 10 kN load cell. The strain was measured with an extensometer with 50 mm gage length. In addition, strains were monitored by digital image correlation (DIC). An artificial speckle pattern was created with black and white paints in order to monitor de displacements on the specimen's surface. A commercial DIC system from Correlated Solutions, model VIC-2D 2009 was used for this purpose. Images with a 2452×2056 pixels definition were stored with an 8-bit format and the processing system allowed to measure surface displacements with a spatial resolution of ≈80 μm/pixel through a CCD camera (stingray F-504 from Allies vision technologies). Both techniques provided equivalent results. The shear stress and shear strain were obtained according to the ASTM D3518/D3518M-94(2001) Standard Test Method for "In-plane shear response of polymer matrix composite materials by tensile test of a ±45° laminate".

Two specimens were loaded monotonically until failure and one was periodically unloaded and reloaded at different strains to determine the evolution of the elastic modulus with deformation. Finally, another two specimens, denominated S1 and S2, were loaded up to a given strain. The tests were stopped and the specimens were immersed in a dye penetrant liquid during 30 min while holding the displacement constant to enhance the contrast between the cracks and the composite material. The liquid was composed of 60 g of ZnI in 10 ml of water, 10 ml of ethanol and 10 ml of Kodak Photo-Flo 200. The specimens were removed from the machine and inspected by XCT as detailed below. Afterwards, the samples were taken back to the testing machine and reloaded to the next step. The whole procedure was repeated several times in both specimens. It should be noticed that the shear stress–strain curve of all the specimens were practically superposed, indicating that neither periodic unloading nor liquid immersion modified the laminate properties.

3. X-ray computed tomography

The spatial distribution of the deformation and failure mechanisms was studied by XCT using a Nanotom 160NF (Phoenix). The tomograms were collected at 90 kV and 100 μA using a tungsten target. For each tomogram, 2000 radiographs were acquired with an exposure time of 750 ms. Tomogram voxel size was set approximately to 10 μm/voxel. The tomograms were then reconstructed using an algorithm based on the filtered back-projection procedure for Feldkamp cone beam geometry. The damage in the reconstructed volumes was qualitatively and quantitatively analyzed using the freeware ImageJ software and subroutines written in Matlab. Accurate quantification of crack number, density and degree of rotation was possible because of the use of a dye penetrant liquid containing ZnI which caused the cracks to appear brighter in the tomograms due to the higher X-ray absorption coefficient of ZnI as compared with the carbon fibers or the polymeric matrix.

3.1. Automatic evaluation of fiber rotation

An automatic procedure was developed to analyze damage development (fiber rotation and matrix cracking) once the pre-processing of one sample set was complete, including the tomographic volumes obtained after deforming the specimen at different strain levels. The procedure was performed in two steps.

The evaluation of fiber angles in non-cracked specimens was determined through the evaluation of fiber bundles which were visible when cracks were not present. The identification of single fibers was not possible since the resolution used for these relatively large specimens was not high enough. Rotation angle evaluation in cracked specimens was based on the rotation of intralaminar matrix cracks, which are inherently linked to the rotation of fibers. In the present case, the specimens were scanned after unloading and therefore the fiber rotation corresponds to the contribution of the inelastic strain (a combination of damage and plastic strain). However, the elastic contribution to fiber rotation at a certain point of the stress–strain curve can be calculated considering the actual elastic properties which can be obtained from periodic unloading tests.

Fiber bundles (or cracks) were segmented and fitted in 2D with ellipses of equal area and moment of inertia. Using this approximation, the semi-axes of the fiber bundles can be determined from the eigenvalues of the moment of inertia tensor (principal moments of inertia). The orientation of the each fiber bundle (or crack) was characterized by the angle between the principal axes of the equivalent ellipse (corresponding to the minimum principal moment of inertia) and the loading direction (reference axis). The average of the orientation angle of all the fiber bundles (or cracks) was used as the absolute fiber orientation of the ply. In order to avoid errors arising from the small misalignments during sample rotation to the reference axis, the difference of the average orientation angles between two consecutive plies was computed and followed through the different loading stages. In this way it was possible to automatically evaluate the changes in orientation in fiber bundles and

intralaminar matrix cracks (and therefore the fibers orientation change) of the whole laminate as well as the differences in orientation angle throughout the laminate, i.e. every two plies.

3.2. Automatic evaluation of matrix cracking

The second step in the procedure concerned the automatic evaluation of the nucleation of cracks and their distribution. To this end, the cracks have to be identified in the slice. The Hough transform has been used for this purpose. The Hough transform is a feature extraction technique used in image analysis, computer vision, and digital image processing [22,23], which is aimed at finding imperfect instances of objects within a certain class of shapes by a voting procedure. This voting procedure is carried out in a parameter space, from which object candidates are obtained as local maxima in a so-called accumulator space that is explicitly constructed by the algorithm for computing the Hough transform.

A Matlab code was written to characterize the cracking patterns on individual plies. The code used the Hough transform to find the features (cracks) within the ply. All evaluations for intralaminar cracks were performed in the central part of ply (a region composed of 850 × 850 pixels – about 8.5 × 8.5 mm^2) where the crack pattern was not influenced by edge effects. The different outputs of the algorithm are shown in Fig. 1. Fig. 1(a) shows the central part of an external ply of the specimen S1 deformed up to a shear strain of $\gamma = 0.107$ (63.4 MPa). Most of the cracks encompass the whole ply in the portion of the slice selected and only a few of them start at one edge but do not cross the ply. The developed algorithm was not influenced by this behavior and it was able to select partial

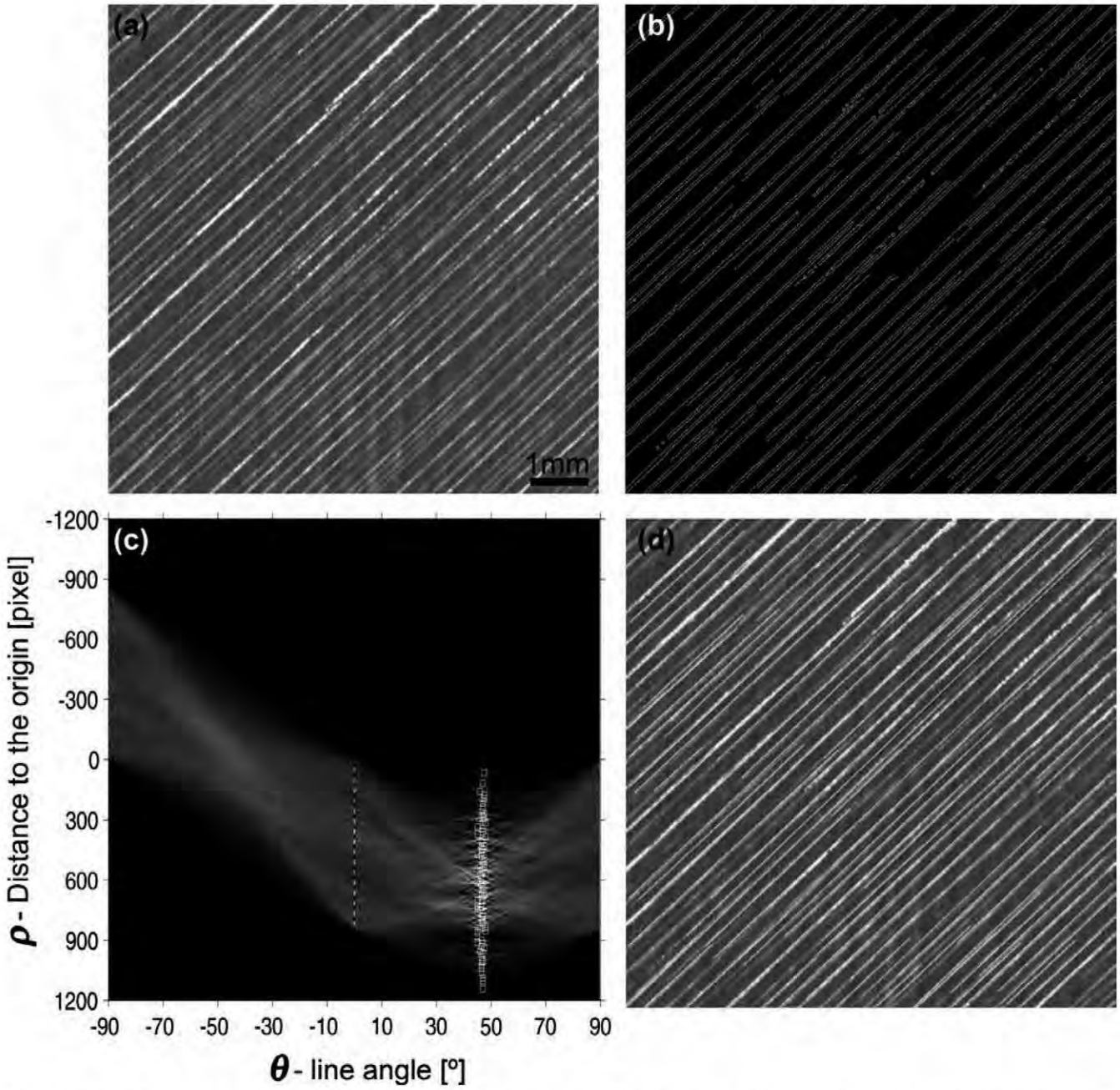

Fig. 1. Several stages of the crack segmentation algorithm. (a) Central part of an external ply of the specimen S1 deformed up to a shear strain $\gamma = 0.107$ (63.4 MPa)–point 3–. (b) Result of the edge detection algorithm of (a). (c) Hough transform of the edge-filtered image. (d) Lines depicted over the cracks in the real space.

cracks as long as their length was above an arbitrary minimum length.

The Canny edge detection algorithm was first applied to the tomographic images of each ply and the results corresponding to Fig. 1(a) are shown in Fig. 1(b). The Canny method applies a high threshold for low edge sensitivity and a low threshold for high edge sensitivity. Compared with other edge filters the Canny method has performed better filling in the gaps in the detected edges. The high threshold was automatically selected based on an iterative procedure performed on the input image to obtain the best combination between minimum noise and maximum crack detection. The criteria used for the high threshold selection was based on the ratio between the number and length of features with different orientation resulting from the Canny edge detection procedure, since for low values of high threshold the picked-up noise is usually randomly oriented while cracks have a preferential orientation. The low threshold value was kept equal to 40% of the high threshold value for all the cases.

Once the crack edges are detected, they can also be quantified, even if only part of the crack is detected, as long as their length is above a minimum value. Contrast fading between matrix and cracks occurs when cracks with openings less than the tomographic resolution are filled with the dye-penetrant. According to [24], crack openings of about 5% of the reconstructed voxel size can be detected using the dye penetrant technique. However, the Canny edge detection algorithm was able capture low contrast cracks and provides a better crack segmentation, since it is based on the local maxima of the gradient of the image (the gradient is calculated using the derivative of a Gaussian filter). On the other hand, it provides two edges per crack (Fig. 1b) and the selection of one line (crack) every two edges is considered in a later step, after transformation of the edge filtered image into the Hough space.

In the Hough space, a line is defined in terms of its parameters instead of a series of points. Two parameters are used to define a line, the shortest distance to the origin (located in the upper right corner in Fig. 1a), ρ, and its angle with respect to the horizontal, θ. Fig. 1(c) shows a typical Hough transform of the edge filtered image in Fig. 1(b). The sinusoids observed in the Hough space are related to points of the objects in the original image space (crack edges and/or noise). When points form a straight line in the original image space, the sinusoids will cross at the parameters of the lines in the Hough space. The intensity of the point where the sinusoids cross will increase with the length of the straight line in the original image space. A threshold value of 0.05 of the maximum intensity was selected in order to avoid spurious crack detection due to lack of intensity of the points in the Hough space allowing to detect cracks larger than 1 mm. Then, line parameters are selected according to the intensity of the points (or peaks) aided by the angle of the known line direction, i.e. +45° or −45°. After the peak is identified, a window of a certain size is set to zero around each peak to avoid the selection of a second peak coming from the same crack as the Canny method provides two edges per crack. A square around the selected peaks is plotted in Fig. 1(c).

Once this procedure is completed, the obtained parameters can be used to depict the lines in the original image space over the original slice. This is shown in Fig. 1(d) where the green lines (obtained from the Hough transform procedure) are superimposed with the real cracks. The cracks in the upper left corner and in the lower right corner of Fig. 1(d) are not detected by the algorithm since the intensity contribution from these short lines was below the threshold selected for peak segmentation in the Hough space. However, they were not relevant for the quantification performed.

The selected lines (corresponding to intralaminar cracks) can be used to quantify matrix cracking. The average distance between consecutive cracks can be calculated as $d = dmax/(N-1)$ where N is number of cracks and $dmax$ the distance between the first and the last crack. The crack density was obtained as $N/dmax$. The average of the orientation angle of all the cracks was evaluated from the θ parameter of the lines and it was coincident within an error of ±0.1° with the orientation obtained following the method described in Section 3.1.

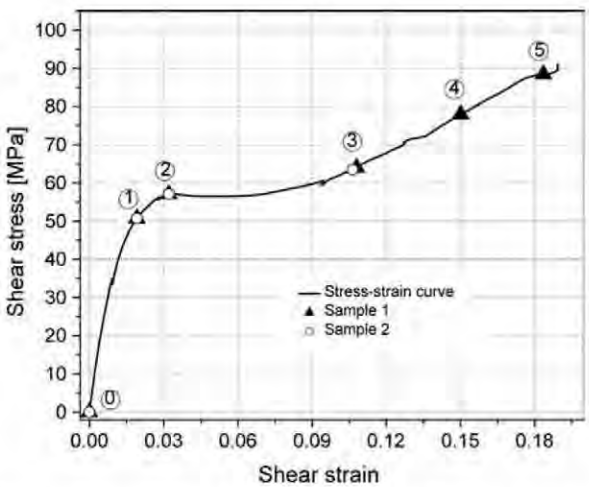

Fig. 2. Shear stress–strain curve of the $[\pm 45]_{2S}$ laminate. The triangular (specimen S1) and circular (specimen S2) marks in the curve correspond to the instants when the specimens were examined by XCT.

4. Results and discussion

The shear stress–shear strain curve obtained from the tensile test of a $[\pm 45]_{2s}$ carbon fiber laminates is shown in Fig. 2. Three different regions can be identified in the stress–strain curve. The initial elastic region with high stiffness up to the proportionality limit (point 1), in which damage was not observed. This is followed by a plateau, in which the stress remains practically constant. A third region appears after the plateau, in which the shear stress increases with the applied shear strain. The slope of the shear stress–shear strain curve in the third region is nearly constant until fracture.

The degradation of the laminate stiffness with the applied strain was studied with one test in which the specimen was periodically unloaded and reloaded, as shown in Fig. 3(a). For the sake of clarity, only one complete unloading–reloading cycle is shown. The degradation of the laminate shear modulus was obtained according to [3] from the slope of the dashed line in Fig. 2(a) for each unloading–reloading cycle. Since the unloading–reloading cycles are non-linear the value obtained from the slope is an apparent shear modulus that includes viscoelastic, rheological and other effects. This procedure allowed us to compare the change of apparent shear modulus during shear deformation. The evolution of the laminate apparent shear modulus with the applied strain is shown in Fig. 3(b). A large reduction was found beyond the proportionality limit (≈1.5% shear strain) and the minimum value of the apparent shear modulus was reached shortly after the end of the plateau region (≈12% shear strain). From this point, the apparent shear modulus increased linearly with strain until catastrophic failure occurred at a shear strain of ≈20%.

The changes in the apparent shear modulus with strain come about as a result of the deformation and damage mechanisms which develop upon deformation. These phenomena can be quantified in each ply by means of XCT using the techniques presented above. To this end, two specimens (S1 and S2) loaded up to different strains were examined by XCT after immersion in a dye penetrant liquid. Specimen S1 was subjected to five XCT scans in points

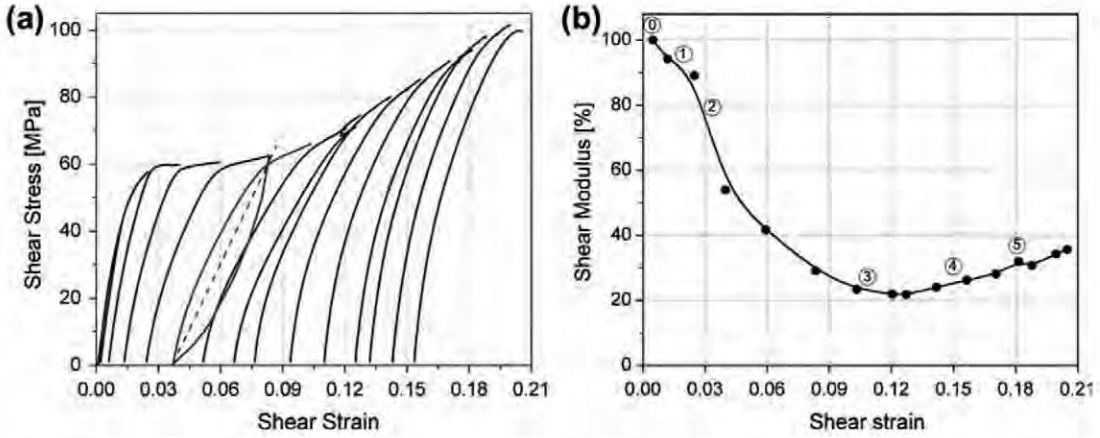

Fig. 3. (a) Reloading cycles in the specimen subjected to periodic unloading–reloading. Only one full unloading–reloading cycle is depicted in blue. (b) Evolution of the laminate shear modulus (divided by the initial modulus) as a function of the applied strain. The points 0 to 5 indicate the strains at which tomographic measurements were performed. The shear modulus of the undamage laminate was 4.925 GPa. (For interpretation of the references to colour in this figure legend, the reader is referred to the web version of this article.)

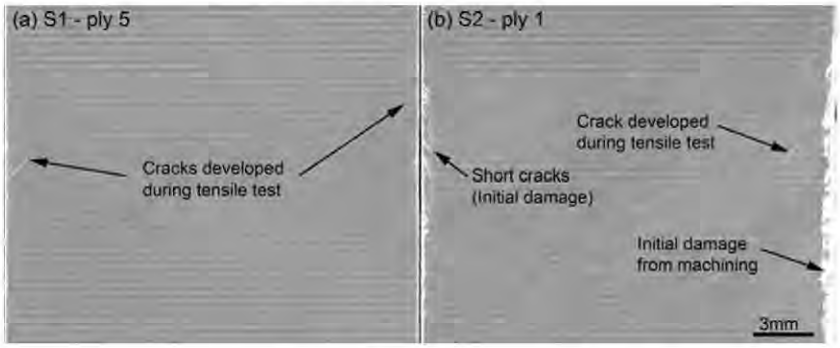

Fig. 4. (a and b) XCT slice of ply 5 and 1 of specimens S1 and S2, respectively, deformed up to point 2 ($\gamma = 0.032$) (57.1 MPa). Very small cracks emanating from the edges of the sample are visible as well as initial damage in sample S2.

1 to 5 while specimen S2 was scanned in points 1, 2 and 3 (Fig. 2). The tomographic measurements were performed for all the loading stages (including the initial state) in the central part of the test coupons since no previous information of the final fracture location was available. Fracture occurred far away from the grips but outside the central part in the scanned specimens.

4.1. General observations

Visual inspection of the volumes was performed after reconstruction of the two sets of samples. The two specimens were scanned before loading to identify any damage produced by machining. No damage was found in S1, while delamination and short matrix cracks were observed at the edges of S2 between the two outermost plies (plies 1 and 2, and plies 6 and 7) (Fig. 4b). The initial damage, probably introduced during machining, was symmetrically distributed with respect to the loading axis and to the middle ply plane (Fig. 4b). Despite the initial damage, the mechanical response of specimen S2 was identical to that of specimen S1 up to point 3 in Fig. 2.

The inspection of the tomographic data after loading up to point 2 in Fig. 2 revealed that cracks appeared in both specimens above the proportionality limit, at shear strains between $\gamma = 0.019$ (50.7 MPa) and $\gamma = 0.032$ (57.1 MPa). Short cracks emanating from the laminate edge were sparsely distributed along each ply and were observed on several plies in both samples loaded up to a shear strain of $\gamma = 0.032$ (57.1 MPa – point 2), as observed in Fig. 4. The limited reduction in the apparent shear modulus in this region, Fig. 3(b), is compatible with the formation of these short cracks although it should be noticed that the resolution of the tomograms (voxel size ≈10 μm/pixel) was not ideal to detect incipient small cracks, even if they are filled with the dye allowing to detect openings of about 5% of the reconstructed voxel size [24].

The development of matrix cracking in each ply can be qualitatively ascertained in the tomograms obtained after the specimen was deformed up to different shear strains. This evolution is depicted in Fig. 5 for plies 1, 2, 3 and 4 of specimen S1. The cracks were filled with ZnI and appeared brighter in the tomograms due to the higher X-ray absorption coefficient of ZnI in comparison with the carbon fibers or the polymeric matrix. The crack density (clearly visible from a shear strain of $\gamma = 0.107$ (63.4 MPa – point 3 in Fig. 2) increased with the applied strain, as expected.

Both specimens showed the same damage features throughout the lamina despite the initial damage in specimen 2. All the inner plies presented cracks crossing the whole ply as well as shorter cracks developing from both edges towards the center of the each lamina but not crossing the whole ply. Shorter cracks grew from the edges with the applied strain until they met near the center of the ply. This effect was observed up to shear strains as high as $\gamma = 0.15$ (77.9 MPa – corresponding to point 4) in the inner plies, in which matrix cracking has not reached saturation, but it should take place earlier in the external plies (between points 2 and 3 in Fig. 2) since they showed cracks going through the whole lamina in point 3.

The accumulation of damage by matrix cracking at the edges is clearly visible in Fig. 6 which shows a 3D rendering of specimen S1

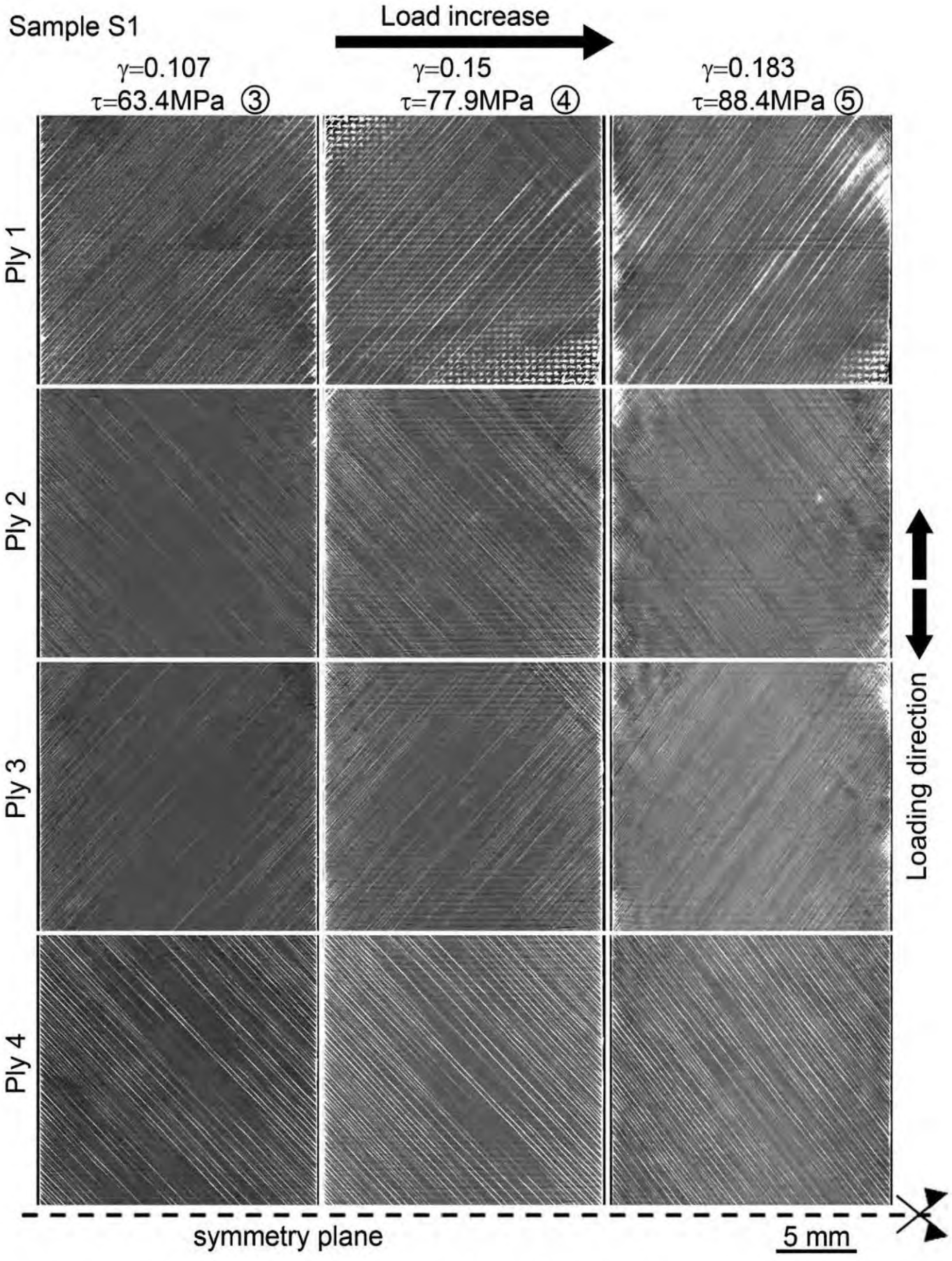

Fig. 5. Matrix crack pattern in the different plies of specimen S1 as a function of the applied shear strain.

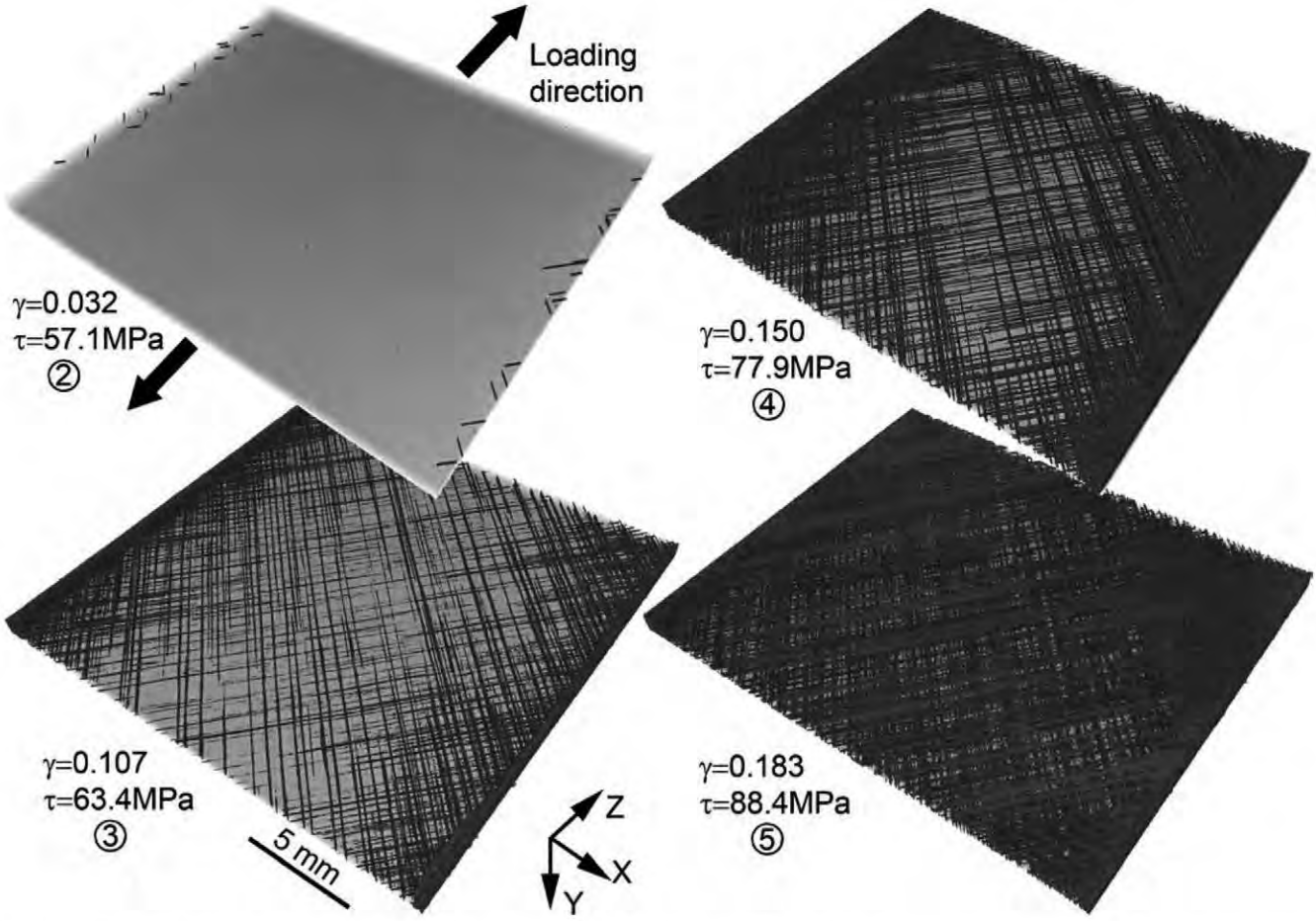

Fig. 6. 3D reconstruction of the tomographic volumes of specimen S1 after deformation at different loads. Damage is shown in red and the composite material in semitransparent. Outer plies were partially removed for clarity. (For interpretation of the references to colour in this figure legend, the reader is referred to the web version of this article.)

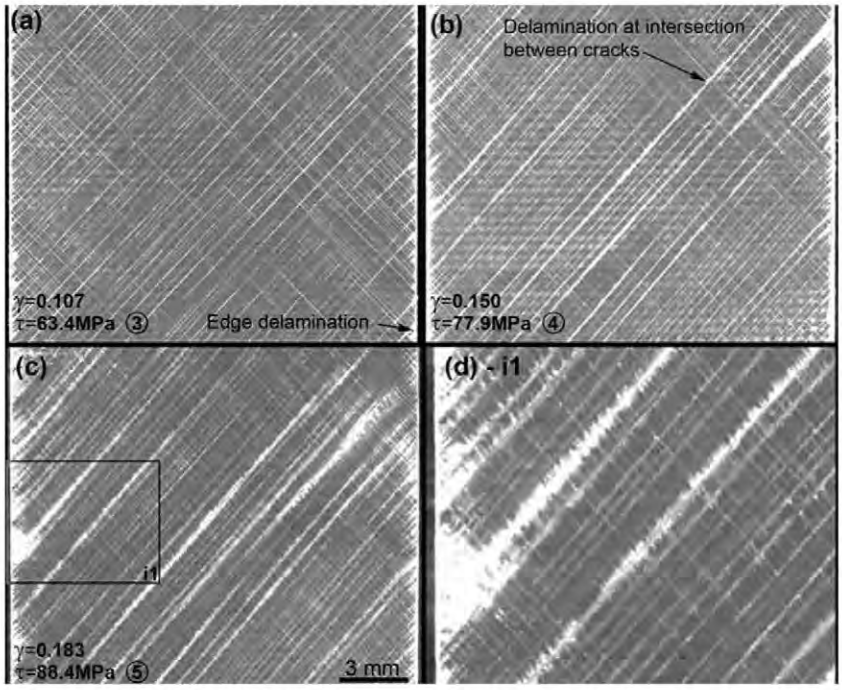

Fig. 7. Interply delamination obtained from the projection of the maximum gray level perpendicular to the slices from plies 1 and 2 of specimen S1. (a) Point 3. (b) Point 4. (c) Point 5. (d) Detail of the inset i1 in (c). The same pattern was observed in the symmetrical interply (plies 6 and 7).

deformed up to different loads. The cracks are shown in red and the outer plies where partially removed for the sake of clarity. The polymeric matrix and the carbon fibers were set to semitransparent grey color to allow visualization inside the specimen. As mentioned above, the quantitative analysis of the crack density is focused in the central part of the plies to eliminate the edge effect.

Obviously, matrix cracking in the plateau region of the shear stress–strain curve (between points 2 and 3 in Fig. 2) was responsible of the dramatic reduction by ≈80% in the laminate apparent shear modulus (Fig. 3b). It is important to notice that the apparent shear modulus (as well as the shear stress) increased with the applied strain beyond point 3 although the density of matrix cracks also increased, as it is clearly seen in Figs. 5 and 6. This behavior can only be induced by the rotation of the fibers, which take up more load as they become aligned with the loading axis.

In order to visualize interply delamination, Fig. 7(a–c) show images corresponding to points 3, 4 and 5, respectively, of specimen S1 with superimposed information (projection of the maximum gray level) from plies 1 and 2 and their interface in the direction perpendicular to those plies. Delamination between plies was first observed at the edges of the specimen S1 at point 3, corresponding to a shear strain of $\gamma = 0.107$ (63.4 MPa) (Fig. 7a). No delaminations were observed at crack intersections at ply interfaces at point 3 but only small edge delaminations (Fig. 7a). Edge delamination did not propagate form the borders in the following loading steps but small new delaminations developed at the intersection of cracks between consecutive plies along the whole interply surface (Fig. 7b) and this process was more relevant at higher stresses (Fig. 7c). The inset in Fig. 7(d) (marked as i1) shows a detail of a delamination developed at the edge and at the intersection between matrix cracks in both plies. A similar pattern was observed in the symmetric interface (between plies 6 and 7). Interply delamination between plies 2 and 3 (and its symmetric interface 5 and 6) was almost nonexistent during the whole mechanical test. Interply delaminations between plies 3 and 4, and 4 and 5 occurred at crack intersections but to a smaller extent when compared to the outer plies. The small delaminated areas did not allow a reliable quantification of this damage mechanism.

Tomographic scans of the laminate were carried out in the central section of the specimens due to the limited field of view of the detector at the selected resolution. Specimens deformed up to point 5 in Fig. 2 showed severe edge delamination above the scanned region, particularly between plies 1 and 2 and 6 and 7, and an additional XCT inspection was performed in this region. A 3D rendering of damage in the fracture region just before failure is depicted in Fig. 8(a), showing extensive delamination. The sample finally fractured at this position at a shear strain of $\gamma = 0.19$ and a shear stress of ≈90 MPa. Regarding the rest of the interfaces, the same observation for the central portion of the sample regarding delamination holds for the final fracture position. Large local deformation with fiber rotation was only observed at the final fracture position in the plies which showed the smallest damage by delamination from the edge and at crack intersections, i.e. at plies 3 and 5 (Fig. 8b).

4.2. Fiber rotation

Using the automatic procedure presented above, the residual fiber orientation was determined for each ply of both specimens at different loading stages. The residual fiber angle between

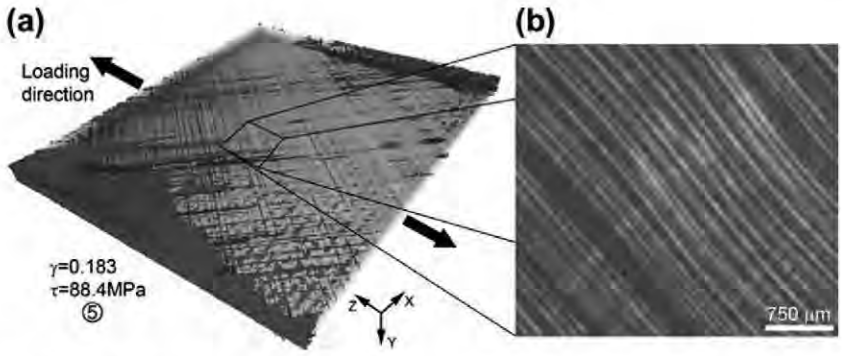

Fig. 8. Tomographic reconstruction of specimen S1 at the fracture region just before failure. (a) 3D rendering of the laminate at a shear strain $\gamma = 0.183$ (88.4 MPa) (just before fracture) showing extensive delamination at the edges. (b) Localized fiber rotation in ply 5.

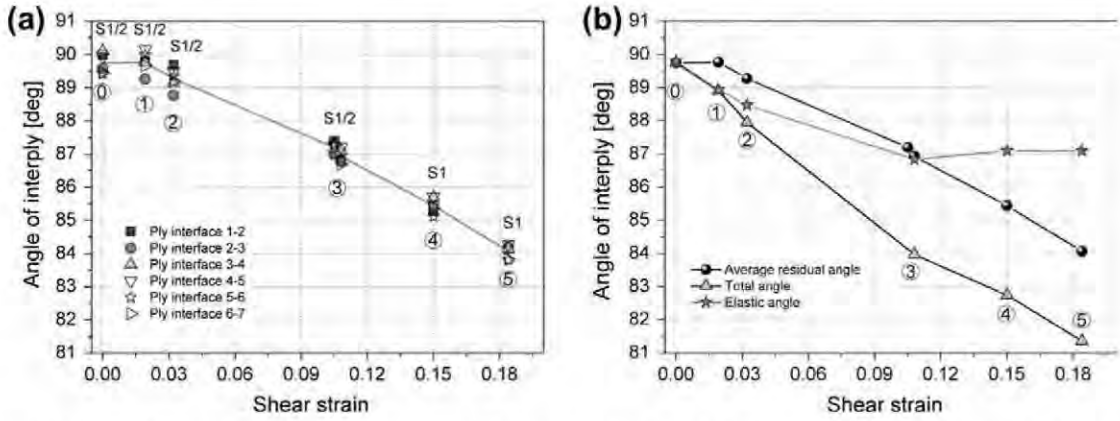

Fig. 9. (a) Evolution of the residual fiber angle every two consecutive plies with the applied shear strain for specimens S1 and S2. (b) Evolution of the average residual rotation for all the plies, the contribution to rotation due to the elastic deformation and the total rotation (residual + elastic) as a function of the applied shear strain.

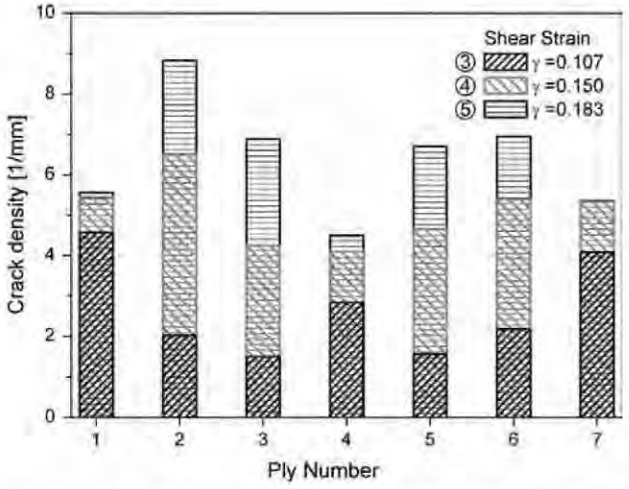

Fig. 10. Crack density in each ply as a function of the applied load. Results for points 3, 4, and 5 of specimen S1.

consecutive plies for specimens S1 and S2 is shown in Fig. 9(a). Both decreased (rotation towards the loading axis) from about 89.8° to about 84.1° in the central region. The initial residual fiber angle between consecutive plies was close to 90° and remained constant up to point 1 in Fig. 2, just at the end of linear region in the shear stress–strain curve. After this point, fiber angle between consecutive plies decreased linearly up to the failure point. The residual fiber rotation of specimen S2 (which contained initial damage) was similar to that of specimen S1 up to point 3 in Fig. 2.

The residual rotation was also measured at the fracture position (where extensive delamination occurred) at a shear strain of $\gamma = 0.183$ (88.4 MPa), just before fracture. The rotation of the fibers at this position was equal -within the experimental error- to that found in the central portion of the laminate. This result indicates that damage by delamination does not influence the residual angle, which was controlled by inelastic deformation within the ply. In addition, the amount of fiber rotation was similar for all the plies indicating that it is not affected by the inhomogeneous distribution of other damage mechanisms, such as matrix cracking or delamination, through the laminate thickness.

The elastic contribution to the fiber angle between the adjacent plies ($2\theta_e$) was computed as:

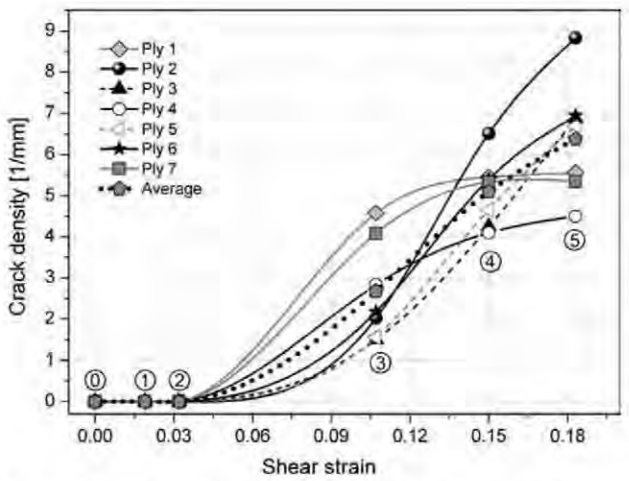

Fig. 11. Evolution of matrix crack density in each ply as a function of the applied shear strain of specimen S1.

$$2\theta_e = 2arctan\left(tan(\theta_0)\left(1+\varepsilon^e_{yy}\right)/\left(1+\varepsilon^e_{xx}\right)\right) \quad (1)$$

where θ_0 is the fiber angle in the unloaded state and ε^e_{xx} and ε^e_{yy} are the elastic axial and transverse strains, respectively, obtained from the DIC measurements during the reloading parts of the test with periodic loading–unloading. The elastic axial, ε^e_{xx}, and transverse, ε^e_{yy}, strains correspond to the difference between the global axial and transverse strains and the permanent shear strain built up during consecutive cycles, respectively. The non-linearities during the unloading–reloading cycles were not considered in the calculation of the elastic contribution to the fiber angle, but their effect is negligible.

The evolution of the elastic contribution to the fiber angle is plotted in Fig. 9(b), together with the average residual rotation, and the total rotation obtained by adding the elastic and the residual contributions. The elastic rotation angle decreased up to point 3 and remained practically constant from this point on, following the overall evolution of the apparent shear modulus with the applied strain. The total rotation decreased nearly linear with the applied strain from 89.8° to 81.4°.

4.3. Crack density

The density of matrix cracks in each ply in the central part of the laminate was measured following the procedure presented above in a square region of 850 × 850 pixels which covers about 25% of the total scanned area. The crack density in the each ply (1 and 7 are the external plies while 4 is the central ply) of specimen S1 is plotted in Fig. 10 for three different values of the applied shear strain corresponding to points 3, 4 and 5 in Fig. 2. The highest crack density at point 3 ($\gamma = 0.107$) was found in the external plies and it did not increase significantly with further deformation. The minimum crack densities at this loading stage were found in the inner plies 2, 3, 5, and 6, located between the external plies and the central ply, while the central ply presented an intermediate crack density. These results can be rationalized in terms of the fracture mechanics analysis proposed by Dvorak and Laws [25] to predict the matrix cracking stress in a ply subjected to in-plane shear. They showed that the *in situ* ply strength was inversely proportional to the square root of the ply thickness and thus, the matrix cracking in the central ply began at lower stresses as compared with the inner plies (2, 3, 5 and 6). In addition, the lack of constrain will also lead to lower cracking stresses in the external plies, as compared with the inner plies.

Further deformation (points 4 and 5 corresponding to $\gamma = 0.150$ and $\gamma = 0.183$, respectively) increased the crack density and the maximum crack density at the end of the test was found in the inner plies (2, 3, 5 and 6). This is in agreement with previous experimental observations [26], which showed that the saturation crack density increased as the ply thickness decreased. In the case of the external plies, lower crack densities at saturation were achieved because of the lack of constraint.

The evolution of crack density in each of the plies as a function of the applied shear strain is plotted in Fig. 11. The average crack density in the external plies did not increased much with deformation from point 3 to point 5, indicating that saturation of matrix cracking occurred during the plateau region of the shear stress–strain curve. The central ply 4 has not reached saturation at the end of the plateau and the crack density increased moderately with the applied strain from point 3 until failure. Finally, the crack density increased very rapidly from point 3 to point 4 in plies 2, 3, 5 and 6 and continued increasing up to point 5 although at lower rate. Thus, these observations indicate that matrix cracking started before point 2 (3% shear strain) and reached saturation around point 4 (15% shear strain) for the external and central plies, while

the inner plies continue cracking. This interval coincides with the region in which the apparent shear modulus decreased with the applied strain. At shear strains above 15%, the apparent shear modulus increased because fiber rotation dominated the mechanical response of the laminate over the matrix cracking mechanisms which was still occurring in the inner plies.

5. Conclusions

The main deformation and damage mechanisms during tensile deformation of $[\pm 45]_{2s}$ carbon fiber–epoxy laminates were analyzed qualitative and quantitatively by means of XCT. To this end, two algorithms were developed for the automatic quantification of matrix cracking and fiber rotation in each ply from the tomograms. The shear stress–strain curve presented three different zones: the initial elastic region led to a plateau up to a shear strain of 9% and was followed by a third region in which the shear stress increased linearly with the applied shear strain until fracture at a shear strain of 19%.

Matrix cracking was first detected at the end of the linear region and progressed rapidly with the applied strain. Matrix cracking was symmetrically distributed with respect to the center of the laminate but the evolution of the crack density depended on the ply location. Matrix cracking started at the external plies which reached saturation at the end of the plateau. The minimum crack density at this stage was found in the inner plies (2, 3, 5 and 6) while the central ply presented an intermediate crack density. Further straining led to further matrix cracking in the inner plies and in the central one and the highest crack density at the end of the test was found in the inner plies, followed by the external plies while the lowest crack density was found in the central ply.

Edge delamination developed initially at the outermost interfaces (plies 1/2 and 6/7) and appeared at the end of the plateau. They did not propagate with further strain and interply delaminations at crack intersection developed mainly at the outermost interfaces during the linear hardening region of the stress–strain curve.

Fiber rotation was detected at the beginning of the plateau region and the fiber angle between consecutive plies decreased linearly with the applied strain until the end of the test. Although damage (matrix cracking and delamination) depended on the ply location, fiber rotation was independent of the ply.

Matrix cracking led to a very large reduction in the apparent shear modulus of the composite, which reached a minimum value of 20% of the initial modulus at the end of the plateau. This reduction partially compensated by fiber rotation in the last stages of deformation and the final apparent shear modulus was 35% the initial one.

Acknowledgements

This investigation was supported by the Spanish Ministry of Science and Competitiveness through the Project MUDATCOM (MAT2012-37552-C03) and by the Comunidad de Madrid through the program ESTRUMAT (S2009/MAT-1585). FS research was supported by the Amarout project, FP7 Marie Curie Action, People-Cofund programme.

References

[1] Hahn HT, Tsai SW. Non-linear elastic behaviour of unidirectional composite laminate. J Compos Mater 1973;7:102–18.
[2] Jones RM, Morgan HS. Analysis of nonlinear stress–strain behavior of fiber-reinforced composite materials. AIAA J 1977;15(12):1669–76.
[3] Van Paepegem W, De Baere I, Degrieck J. Modelling the nonlinear shear stress–strain response of glass fibre-reinforced composites. Part I: Experimental results. Compos Sci Technol 2006;66:1455–64.
[4] Van Paepegem W, De Baere I, Degrieck J. Modelling the nonlinear shear stress–strain response of glass fibre-reinforced composites. Part II: Model development and finite element simulations. Compos Sci Technol 2006;66:1465–78.
[5] Hu HT. Influence of in-plane shear nonlinearity on buckling and postbuckling responses of composite plates and shells. J Compos Mater 1993;27:138–51.
[6] Reifsnider KL, Talug A. Analysis of fatigue in composite laminates. Int J Fatigue 1980;3(1):3–11.
[7] Masters JE, Reifsnider KL. An investigation of cumulative damage development in quasi-isotropic graphite/epoxy laminates. In: Reifsnider KL, editor. Damage in composite materials: mechanisms, accumulation, tolerance, and characterization. ASTM STP, vol. 775. Philadelphia, PA: ASTM; 1982. p. 40–62.
[8] Tong J, Guild JF, Ogin SL, Smith PA. On matrix crack growth in quasi-isotropic laminates – I. Experimental investigation. Compos Sci Technol 1997;57(11):1527–35.
[9] Marsden WM, Guild FJ, Ogin SL, Smith PA. Modelling stiffness-damage behavior of (±45/90)s and (90/±45)s glass fibre reinforced polymer laminates. Plastic, Rubber Compos 1999;28(1):30–9.
[10] Crocker LE, Ogin SL, Smith PA, Hill PS. Intra-laminar fracture in angle-ply laminates. Composites Part A 1997;28(9–10):839–46.
[11] Varna J, Joffe R, Akshantala NV, Talreja R. Damage in composite laminates with off-axis plies. Compos Sci Technol 1999;59(14):2139–47.
[12] Kashtalyan M, Soutis C. Stiffness and fracture analysis of laminated composites with off-axis ply matrix cracking. Composites Part A 2007;38:1262–9.
[13] Wisnom MR. The effect of fibre rotation in ±45° tension tests on measured shear properties. Composites 1995;26:25–32.
[14] Johnson P, Chang FK. Characterization of matrix crack-induced laminate failure-Part I: Experiments. J Compos Mater 2001;35:2009–35.
[15] Rotem A, Hashin Z. Failure modes of angle ply laminates. J Compos Mater 1975;9:191–206.
[16] Wright P, Fu X, Sinclair I, Spearing SM. Ultra high resolution computed tomography of damage in notched carbon fiber-epoxy composites. J Compos Mater 2008;42:1993–2002.
[17] Wright P, Moffat A, Sinclair I, Spearing SM. High resolution tomographic imaging and modelling of notch tip damage in a laminated composite. Compos Sci Technol 2010;70:1444–52.
[18] Sket F, Seltzer R, Molina-Aldareguía JM, Gonzalez C, LLorca J. Determination of damage micromechanisms and fracture resistance of glass fiber/epoxy cross-ply laminate by means of X-ray computed microtomography. Compos Sci Technol 2012;72:350–9.
[19] Hernández S, Sket F, Molina-Aldareguía JM, González C, LLorca J. Effect of curing cycle on void distribution and interlaminar shear strength in polymer-matrix composites. Compos Sci Technol 2011;71:1331–41.
[20] Hernández S, Sket F, González C, Llorca J. Optimization of curing cycle in carbon fiber-reinforced laminates: void distribution and mechanical properties. Compos Sci Technol, 2013, submitted for publication.
[21] Hexcel HexPly M21. <http://www.hexcel.com/Resources/DataSheets/Prepreg-Data-Sheets/M21_global.pdf>. [accessed 18th November 2013].
[22] Hough PVC. Machine analysis of bubble chamber pictures. In: Proc. Int. Conf. High Energy Accelerators and Instrumentation (HEACC), 1959. p. 554–558.
[23] Duda RO, Hart PE. Use of the hough transformation to detect lines and curves in pictures. Comm ACM 1972;15:11–5.
[24] Schilling PJ, Karedla BR, Tatiparthi AK, Verges MA, Herrington PD. X-ray computed microtomography of internal damage in fiber reinforced polymer matrix composites. Compos Sci Technol 2005;65(14):2071–8.
[25] Dvorak GJ, Laws N. Analysis of progressive matrix cracking in composite laminates: II first ply failure. J Compos Mater 1988;21:309–29.
[26] Nairn JA, Hu S, Bark JS. A critical evaluation of theories for predicting microcracking in composite laminates. J Mater Sci 1993;28:5099–111.